

Supporting Information

Heterogeneous Diffusion and Remnant Hardening with Excellent Electromechanical Compatibility in Alkaline Niobate Composite

Hongjiang Li, Ning Chen, Jie Xing, Wenbin Liu, Wei Shi, Hao Chen, Zhi Tan*,
Manjing Tang, Mingyue Mo, Jianguo Zhu*

College of Materials Science and Engineering, Sichuan University, Chengdu, Sichuan,
610064, China.

E-mail address: tanzhi0838@scu.edu.cn (Zhi Tan), nic0400@scu.edu.cn (Jianguo Zhu)

1. Experimental section

1.1. Preparation of KNNT-BNZ-BFO powder

The $0.957(\text{K}_{0.48}\text{Na}_{0.52})\text{Nb}_{0.95}\text{Ta}_{0.06}\text{O}_3-0.04(\text{Bi}_{0.5}\text{Na}_{0.5})\text{ZrO}_3-0.003\text{BiFeO}_3$ (KNNT-BNZ-BFO) powder is synthesized via the traditional solid-state technique. The analytically pure K_2CO_3 (99%), Na_2CO_3 (99.8%), Nb_2O_5 (99.95%), Bi_2O_3 (99.999%), ZrO_2 (99%), Fe_2O_3 (99.99%), and Ta_2O_5 (99.99%) are obtained from Sinopharm Chemical Reagent Co. Ltd., China. Firstly, the analytical grade reagents of high-purity raw materials are mixed by ball milling in a zirconia ball media and anhydrous ethanol solution for 15 to 20 h. Then, the ball-milled powder is pre-sintered at 850 °C for 6 h to obtain KNNT-BNZ-BFO powder. The X-ray powder diffraction (XRD) pattern and X-ray photoelectron spectroscopy (XPS) of KNNT-BNZ-BFO powders are illustrated in [Figs. S1\(a\)](#) and [S1\(b\)](#) match the reported KNN-based ceramics¹⁻³.

1.2. Preparation of CSO powder

The CuSb_2O_6 (CSO) powder is produced by the traditional solid-state technique. The analytically pure Sb_2O_3 (99.99%), and CuO (99%) are obtained from Sinopharm Chemical Reagent Co. Ltd., China. Firstly, the analytical grade reagents of high-purity

raw materials are mixed by ball milling in a zirconia ball media and anhydrous ethanol solution for 15 to 20 h. Then, the ball-milled powder is pre-sintered at 1100 °C for 48 h to obtain CSO powder. The XRD of the synthesized CSO powders matches with the CSO standard PDF cards (PDF#17-0284) and the presence of Sb⁵⁺ and Cu²⁺ in powders is also proved by the XPS test, as shown in [Figs. S1\(c-f\)](#).

1.3. Preparation of KNNT-BNZ-BFO/x CSO composite ceramics

The KNNT-BNZ-BFO/x CSO composite ceramics are fabricated by conventional roll-forming technology. The KNNT-BNZ-BFO and CSO powders are weighed following the stoichiometric formula of KNNT-BNZ-BFO/x CSO and mixed by ball milling in a zirconia ball media and anhydrous ethanol solution for 15 to 20 h. The KNNT-BNZ-BFO/x CSO powders are milled with polyvinyl alcohol (PVA) colloid at a specific mass ratio (for example, 100 g of powder corresponds to 6 g of PVA). The PVA-mixed powders are pressed into plates with a diameter of 14-15 mm and a thickness of 0.18-0.20 mm through the roll-forming process. The PVA is completely burned off at a temperature range of 500 to 550 °C for 3 h. Subsequently, the KNNT-BNZ-BFO/x CSO composite ceramics are sintered through a two-step method. Firstly, they are sintered at 1115 °C for 30 min, and then the temperature is reduced to 1095 °C for 3.5 h. The top and bottom surfaces of the samples are coated with 5 to 15 % weight of silver paste and then fired at 750 °C for 10 min to form electrodes for the measurement of electrical properties. The KNNT-BNZ-BFO/x CSO composite ceramics are polarized in a silicon oil bath at 30 to 120 °C by applying a direct current electric field of 4 to 5 kV/mm for 15 to 20 min.

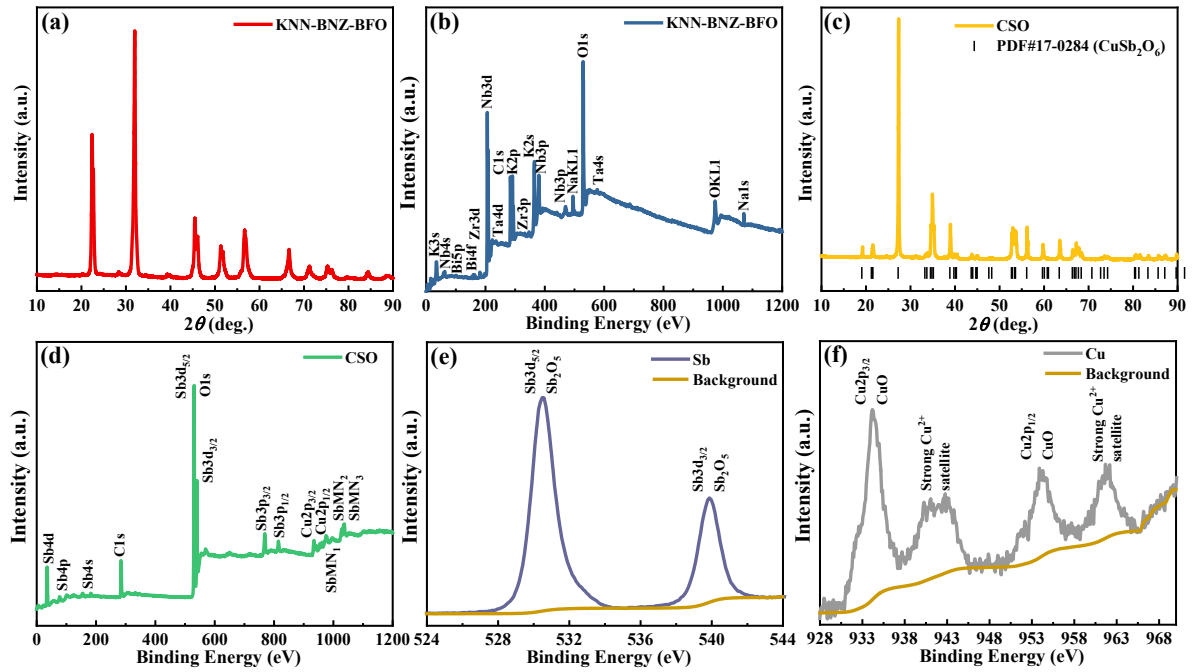


Fig. S1 (a) XRD patterns and (b) XPS full-scan spectra of the KNNT-BNZ-BFO powder. (c) XRD patterns; (d) XPS full-scan spectra; high-resolution XPS spectra of (e) Sb element and (f) Cu element of the CSO powder.

1.4. Sample preparation process for the DMA test

The sample preparation process for the test dynamical mechanical analysis (DMA) is as follows: The KNNT-BNZ-BFO/*x* CSO powders are thoroughly ground to form uniformly distributed particles with 8 *wt.*% PVA as a binder and then pressed into bar-shaped samples with a length of 10-10.5 mm, a width of 6-6.5 mm, and a thickness of 1.8-1.85 mm. The PVA is completely burned off at a temperature range of 500 to 550 °C for 3 h. Subsequently, the KNNT-BNZ-BFO/*x* CSO composite ceramics are sintered through a two-step method. Firstly, they are sintered at 1115 °C for 30 min, and then the temperature is reduced to 1095 °C for 3.5 h.

1.5 Characterization and measurement

The crystal structure and phase purity of the ceramics are confirmed by XRD (Rigaku, D/Max2500, Tokyo, Japan). To confirm the distortion of the BO₆ octahedron and local heterogeneity in the composite ceramics via a Raman spectrometer and Raman mapping, respectively. Raman analysis/Raman imaging is done with a confocal Raman microscope (Alpha300R, WITec GmbH, Germany) equipped with a

TEM single-frequency laser ($\lambda = 532$ nm, laser power = 40 mW, WITec GmbH, Germany). Surface morphology and energy-dispersive spectroscopy (EDS) mapping of the samples are examined using scanning electron microscopy of backscattered electrons (BSE-SEM, S-3400N, Hitachi, Japan). The average grain size (AGS) is analyzed from the BSE-SEM images using a Nanomeasurer program based on over 150 grains. The elemental distributions of the samples are characterized using an electron probe X-ray micro-analyzer (EPMA, 8050G, Shimadzu, Japan). The polished ceramic samples are cut into thin slices using a focused ion beam (FIB, Helios 5 CX, Thermo Scientific Company), and high-angle annular dark field scanning transmission electron microscopy (HAADF-STEM) is performed using a Talos F200S G2 microscopy. A piezoelectric force microscopy (PFM) by a commercial microscope (MFP-3D, Asylum Research, Goleta, CA, USA) is used to characterize the domain structure. The Litho-PFM mode is used in the domain Litho process, during which a positive voltage of 20 V is first applied to the reorientation of the domains in an area of $4 \times 4 \mu\text{m}$, and then a voltage of -20 V is applied to a smaller region ($2 \times 2 \mu\text{m}$) within the poled areas. The potential of the polished samples is characterized by using a KPFM. A micro-electrometer (Keithley 6517B, Keithley, USA) is used to measure the resistivity of the ceramics as a function of temperature. X-ray photoelectron spectroscopy (XPS, AXIS Ultra DLD, Kratos, Japan) is used to determine the elemental valences of the ceramics. A precision impedance analyzer (TH2827, Tonghui Electronic Co, China) is used to measure the temperature dependence of the relative dielectric constant (ϵ_r - T) curves. The nanoindentation method is employed to evaluate the hardness behaviors of ceramics. Mechanical properties are characterized by dynamical mechanical analysis in three-point bending geometry with a Perkin Elmer DMA1 apparatus. The ferroelectric TF Analyzer 2000 (aixACCT, Germany) is used to characterize the current (I - E) loops, the polarization *vs.* the electric field (P - E) behaviors, and the unipolar and bipolar strain *vs.* the electric field (S - E) loops. A quasi-static d_{33} meter (ZJ-3A, Institute of Acoustics, Chinese Academy of Sciences) is used for the piezoelectric coefficient (d_{33}) measurement of the ceramics. The *in-situ* temperature dependence of d_{33} is carried out by using a high-temperature piezometer

(TZQD-D33T, China). The first radial mode frequencies (resonance frequency f_r and anti-resonance frequency f_a), resonance impedance (Z_m), and capacitance at 1 kHz (C^T), phase angle from RT to 290 °C are recorded at regular intervals by an LCR analyzer (Tonghui 2816A, China and HP 4980, Agilent). These parameters are also used to calculate the planar electromechanical coupling factor (k_p) and mechanical quality factor (Q_m) through the following formulas:⁴

$$k_p \approx \sqrt{2.51 \frac{f_a - f_r}{f_a} - \left(\frac{f_a - f_r}{f_a} \right)^2} \quad (1)$$

$$Q_m = \frac{f_a^2}{2\pi f_r Z_m C^T (f_a^2 - f_r^2)} \quad (2)$$

1.6 Phase-Field Simulations

As an approximation, the composite can be considered a dilute solution without the superposition of stress fields⁵. Thus, the model of a single particle in an infinite isotropic matrix can be used to determine the resulting local stress field σ ⁶:

$$\sigma = \frac{\Delta\alpha\Delta T}{\frac{(1+\nu_m)}{2E_m} + \frac{(1-2\nu_s)}{E_s}} \quad (3)$$

where $\Delta\alpha$ is the difference in thermal expansion coefficient between the matrix phase and the secondary phase, ΔT is the cooling range, ν_m , ν_s , and E_m , E_s is the Poisson's ratio and elastic modulus of the matrix phase and the secondary phase, respectively. In the KNNT-BNZ-BFO/ x CSO system, we chose CuNbO₃ (CNO), which is close to the EPMA and STEM characterization results, as the secondary phase and KNNT-BNZ-BFO as the matrix phase. In addition, the construction of the computational model grid map is carried out based on the STEM characterization results. For the KNNT-BNZ-BFO/ x CSO system, $\alpha_{\text{KNNT-BNZ-BFO}} = 12.1 \times 10^{-6} \text{ K}^{-1}$ obtained by calculating the parameters given in the literature⁷, $\alpha_{\text{CNO}} = 32.5 \times 10^{-6} \text{ K}^{-1}$ obtained by calculating the parameters given in the literature⁸, ΔT is estimated to be 1388 K. The $\nu_{\text{KNNT-BNZ-BFO}} = 0.3839$ and $E_{\text{KNNT-BNZ-BFO}} = 41.7023 \text{ GPa}$ are obtained by calculating the parameters given in the literature⁹. The $\nu_{\text{CNO}} = 0.4153$ and $E_{\text{CNO}} = 48.8892 \text{ GPa}$ are obtained by calculating the parameters given in the literature¹⁰. The simulation is carried out by Ansys software, the initial temperature is 1120 °C, and the final temperature is 20 °C. To allow the model to be free to deform and contract during the cooling process, only

horizontal movement is constrained on the left boundary, only vertical movement is constrained on the bottom boundary, and there is no constraint on the right boundary and the top boundary. The number of finite element mesh is 130722 and the number of nodes is 393447. Based on these values, a minimum value of 0.00024047 MPa and a maximum value of 1755.1 MPa for σ at 25 °C are calculated.

2. Results and discussion

In Fig. S2(a-b), it is observed that the intensity ratio and position of the (002) and (200) Bragg peaks around 45°-46° are found to change with the addition of CSO, suggesting that CSO affected the multiphase structure of the ceramics. The position difference of (002) and (200) diffraction peaks gradually decrease, and (002) Bragg peak gradually disappears with the increase of CSO content, which is widely observed in KNN-based ceramics having a high content of Sb-doping and the single peak is reported to be a pseudo-cubic phase^{11, 12}. This is mainly attributable to the replacement of Nb⁵⁺ with Sb⁵⁺ breaking the long-range ferroelectric ordering (LRFO), and the increased replacement of Nb⁵⁺ with Sb⁵⁺ seriously aggravates this process, responsible for the degraded ferroelectric phase. In Fig. S2(c), the (002) Bragg peaks move to high angles and (002) Bragg peaks remain unchanged with the addition of CSO, which implies a decrease in unit cell distortion and increased average crystal symmetry. Raman spectroscopy is performed on samples with different CSO contents to investigate the effect of CSO on the local symmetry of the ceramics, as shown in Fig. S2(d). The ν_1 and ν_5 mode corresponds to the double-degenerate symmetric stretching vibration of the O-B-O bond in the BO₆ octahedron¹³. The ν_1 and ν_5 model wavenumbers show a decreasing trend with the CSO content, as shown in Fig. S2(e). This tendency is due to the decrease in binding strength caused by the shortening of the distance between B-sites and their coordinated oxygen. The trend of the crystal structure parameters observed in KNNT-BNZ-BFO/x CSO ceramics can be understood for the following reasons. These are due to lattice mismatch caused by the smaller ionic radius ($R_{\text{Sb}^{5+}} = 0.61 \text{ \AA}$, $R_{\text{Nb}^{5+}} = 0.64 \text{ \AA}$) and the stronger electronegativity ($\chi_{\text{Sb}} = 2.05$, $\chi_{\text{Nb}} = 1.59$) of Sb⁵⁺ cation compared to the Nb⁵⁺ cation¹⁴.

Thus, the entry of Sb ions into the lattice to replace Nb ions leads to lattice shrinkage. To further investigate the phase structure evolutions of the ceramics with different CSO contents near room temperature, Fig. S2(f) exhibits the temperature dependence of the relative dielectric constant (ϵ_r - T) curves. The presence of a peak in the dielectric constant data around 30 °C indicated the occurrence of a rhombohedral to tetragonal phase-transition temperature (T_{R-T}). However, T_{R-T} is seriously diffused at $x = 0.016$ -0.024 in ϵ_r - T curves, which are ascribed to the vanished energy barriers among different ferroelectric phases¹¹. The R-T phase coexistence together with an abundant domain configuration is likely to flatten the thermodynamic potential curve, which state provides lower polarization anisotropy, enabling easy polarization rotation, and serves as the primary basis for acquiring high piezoelectric properties¹⁵.

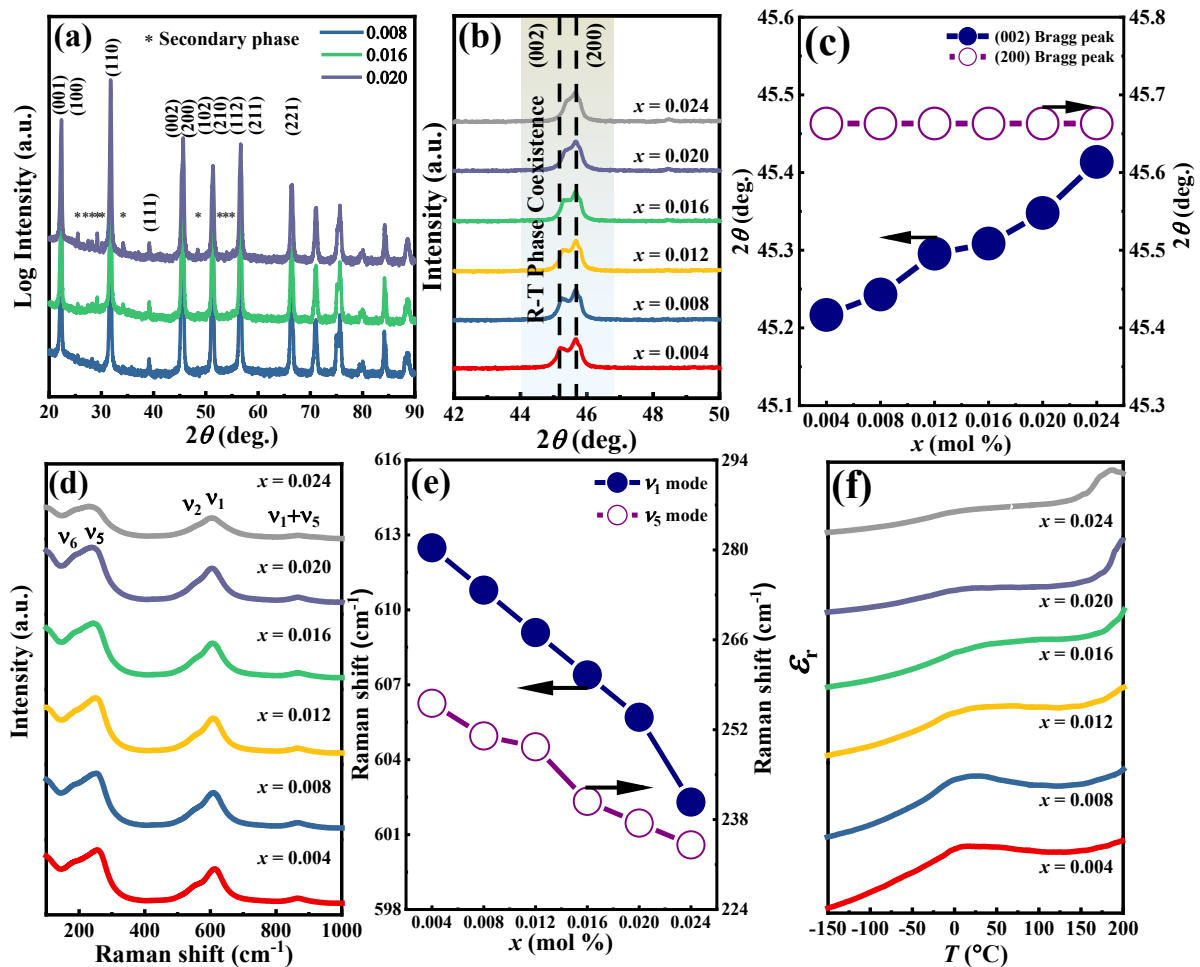


Fig. S2 (a) XRD patterns of the samples. (b) Amplified XRD patterns at $2\theta = 42^\circ$ - 50° . (c) Shift of (002) and (200) Bragg peaks as a function of x . (d) Raman spectra of the ceramics. (e) Raman

shifts of v_1 and v_5 as a function of x . (f) ϵ_r - T curves tested from -150 to 150 °C.

The BSE-SEM images of ceramics are shown in Fig. S3. As x increases from 0.004 to 0.024, the AGS of ceramics shows a decreasing trend. During the sintering process, a secondary phase is generated in the ceramic as the concentration of CSO continues to increase. This decrease in AGS is due to the local stress field impeding the movement of grain boundaries^{2, 16}. BSE-SEM images and corresponding elemental mappings of K, Cu, Nb, Sb, and O are depicted in Fig. S4. The Cu elemental is significantly enriched in the denoted grains as the addition of CSO increases. This implies that a small amount of Nb ions precipitated out of the KNNT-BNZ-BFO phase to form a second phase with Cu ions, while Sb ions entered the lattice to replace Nb ions.

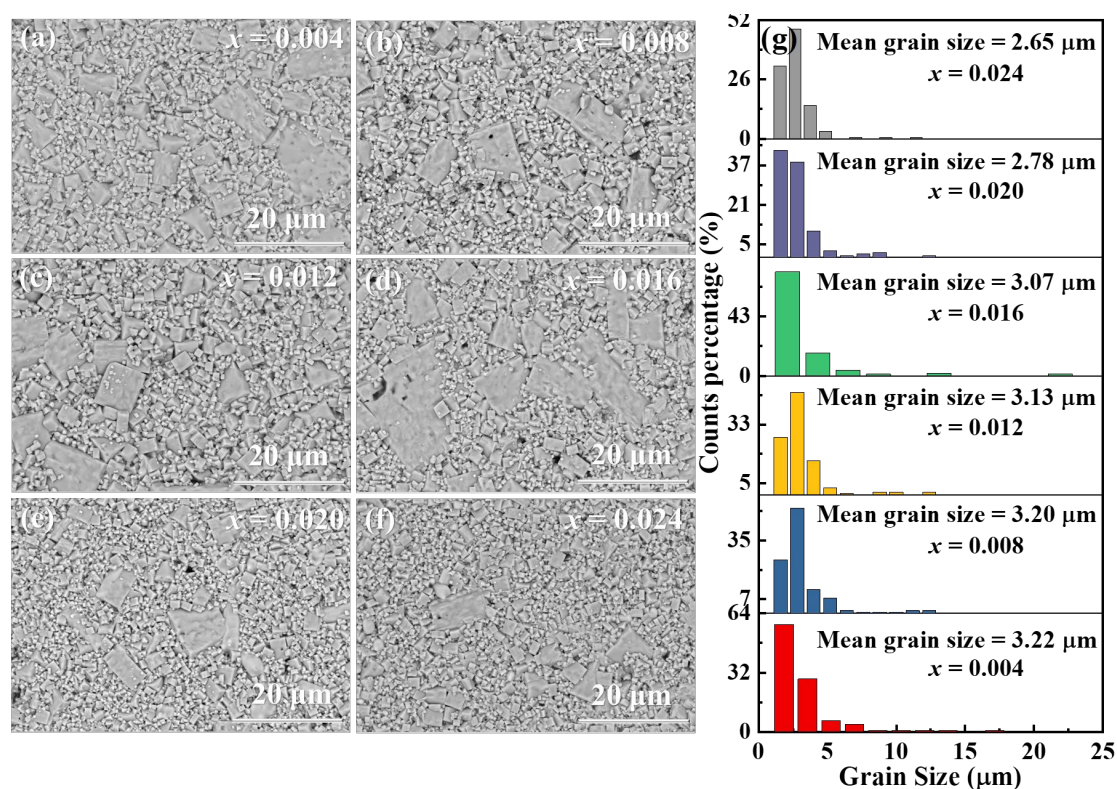
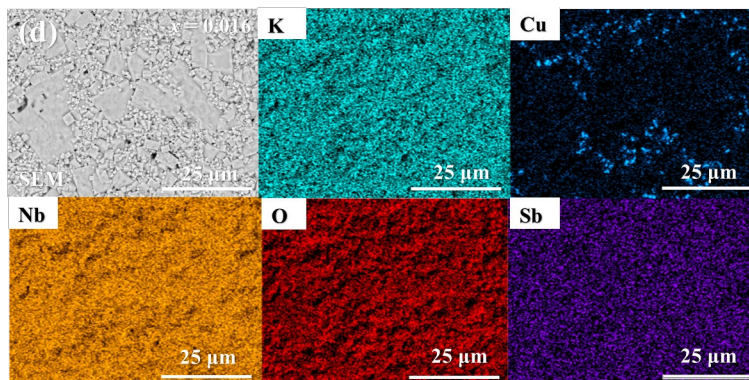
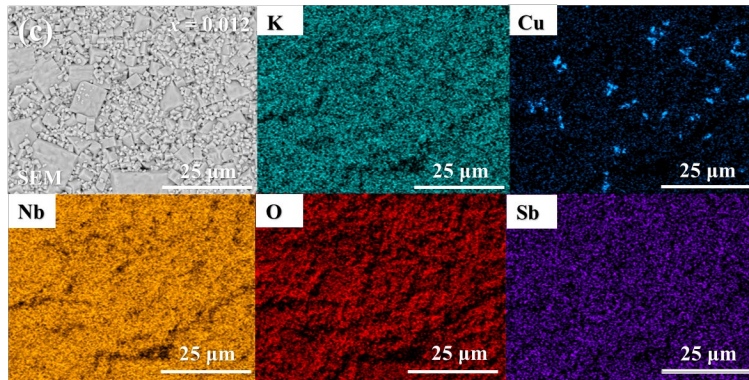
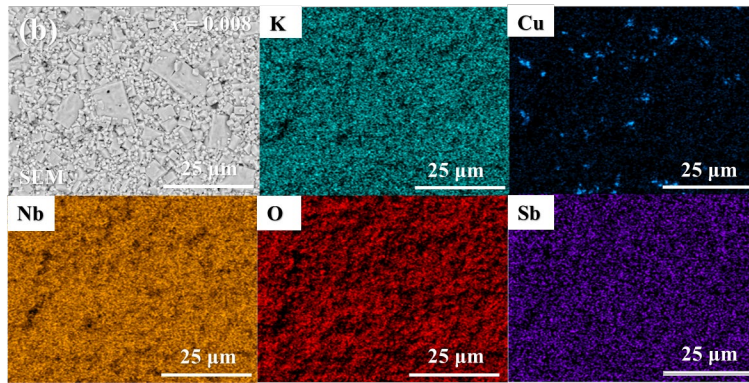
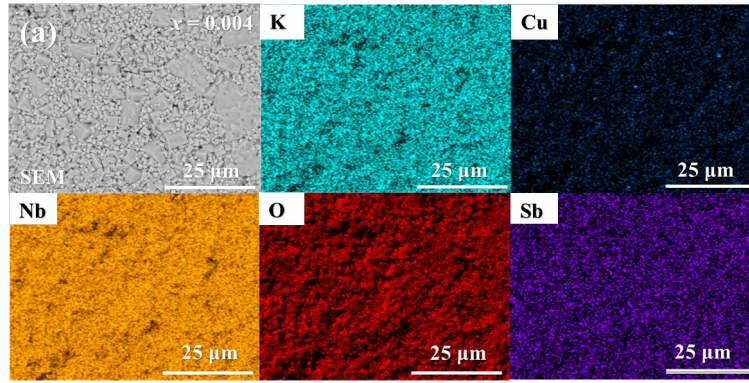


Fig. S3 (a-d) BSE-SEM images of the ceramics with different amounts of CSO. (e) Grain size distribution of each image and variations in the average grain size of the samples.



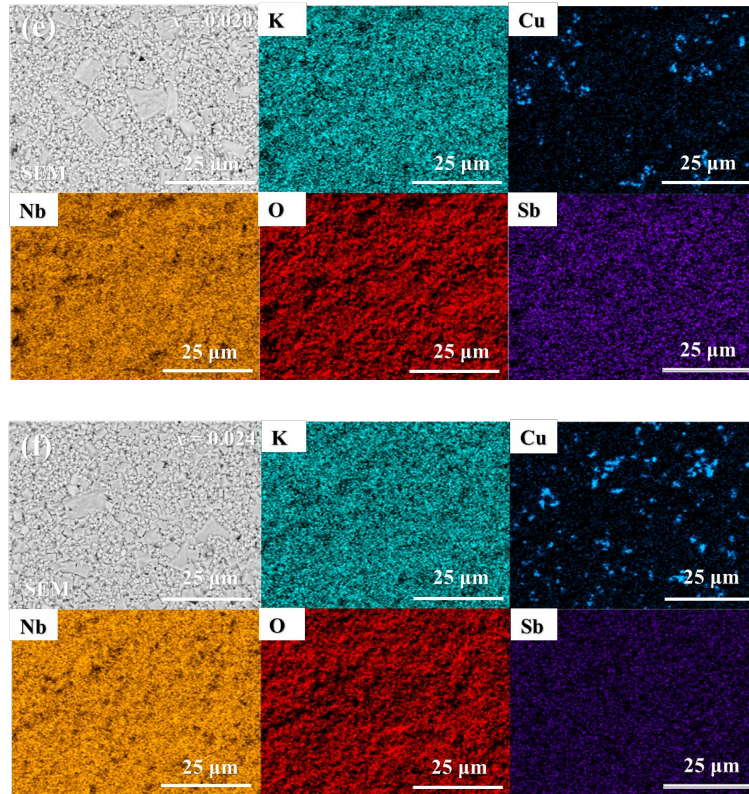


Fig. S4 Mapping images of K, Cu, Nb, O, and Sb elemental for the KNNT-BNZ-BFO/ x CSO composite ceramics.

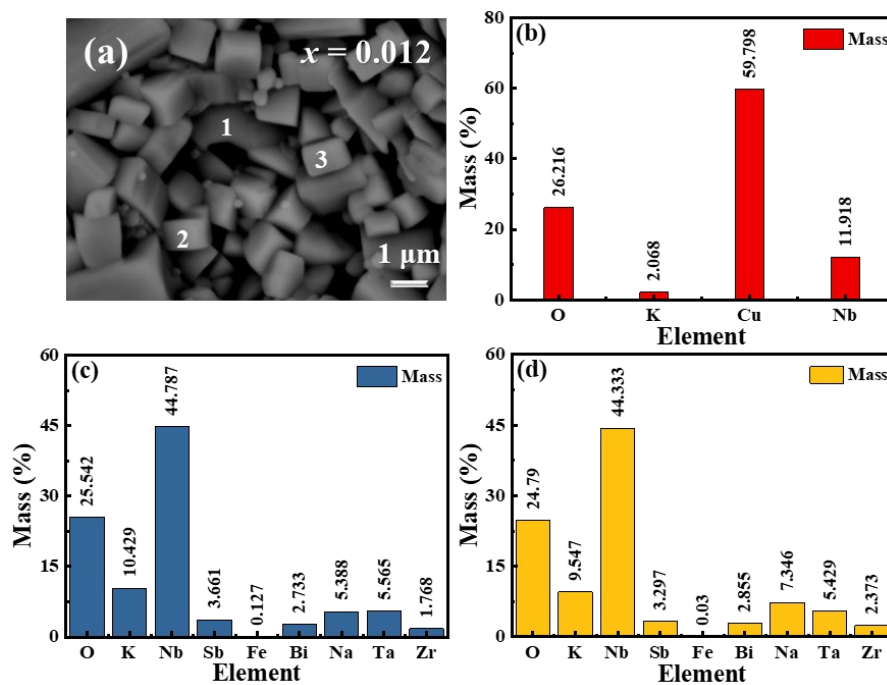


Fig. S5 (a-d) EDS points of the sample and the element mass percentages of the 1, 2, and 3 positions.

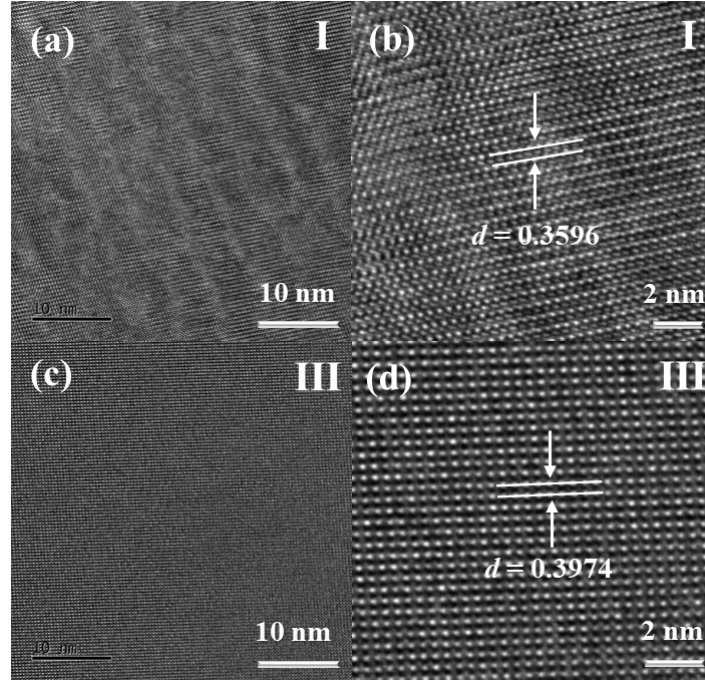


Fig. S6 (a) HR-TEM of the secondary phase (region I) and (b) the IFFT image at the selected area in (a); (c) HR-TEM of the KNNT-BNZ-BFO (region III) and (d) the IFFT image at the selected area in (c).

In addition, Sb ions entering the lattice to replace Nb ions gradually break the LRFO and promote the local structural heterogeneity, which in turn can lead to the formation of extremely miniaturized nanodomains and an enhanced amount of polar nanoregions (PNRs)¹⁷. Fig. S7 shows many micron-scale large domains are broken into nanoscale domains as x increases to 0.012, leading to an increased amount of nanoscale domains. Therefore, compared to samples with $x = 0.004$, samples with $x = 0.012$ show a more complicated domain configuration composed of proper submicron-scale domains and plentiful irregular nanoscale domains, which has been widely observed in the phase-boundary-engineered KNN-based ceramics with high piezoelectricity. Upon further increasing x to 0.024, the large domains are further fragmented, resulting in the dominating but low-density nanodomains.

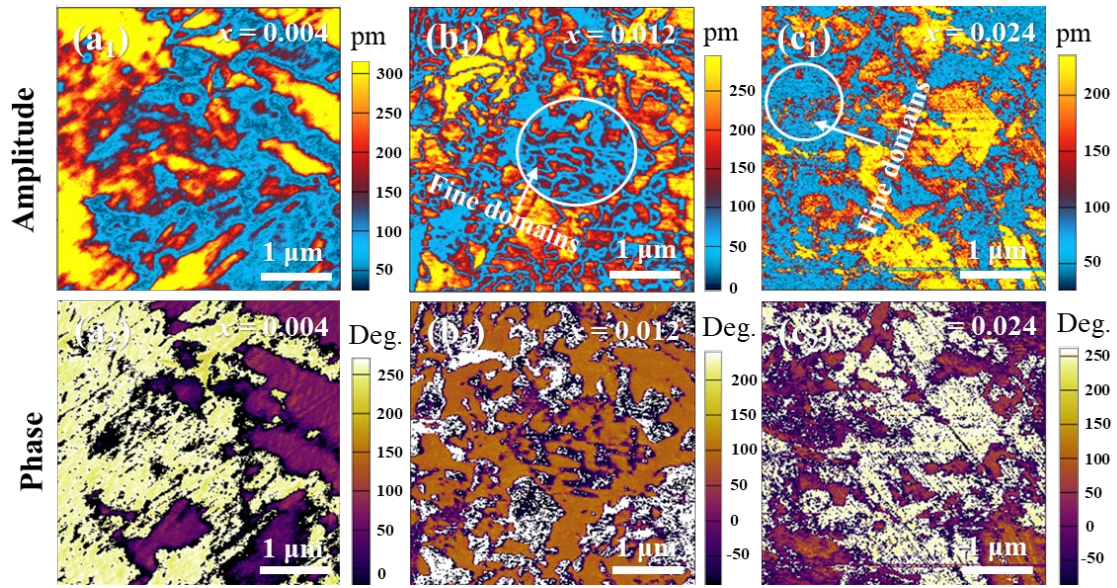


Fig. S7 Domain configurations of the KNNT-BNZ-BFO/ x CSO ($x = 0.004, 0.012,$ and 0.024) ceramics are investigated in detail using out-of-plane PFM. (a₁-c₁) amplitude images of the PFM for the ceramics; (a₂-c₂) phase images of the PFM for the ceramics.

[Fig. S7](#) shows the complex domain patterns with the typical lamellar ferroelectric domains that are observed in the PFM landscapes of the domain structure for the ceramics. The changes in the microstructure of the ferroelectric domain are also closely related to the piezoelectric properties of the material^{18, 19}. [Fig. S8](#) further demonstrates the domain-switching behavior through local polling experiments. A comparison of the amplitudes and phases between the compounds with $x = 0.004, x = 0.012,$ and $x = 0.024$ reveals that domain switching is more pronounced in the sample with $x = 0.024$. It has been reported that PNRs and nano-domains respond more easily to an external electric field compared to micron-domains, facilitating domain wall motion²⁰. The better domain switching behavior at $x = 0.024$ is correlative to the enhanced domain mobility due to the complicated domain configuration including proper submicron-scale domains and plentiful irregular nanoscale domains.

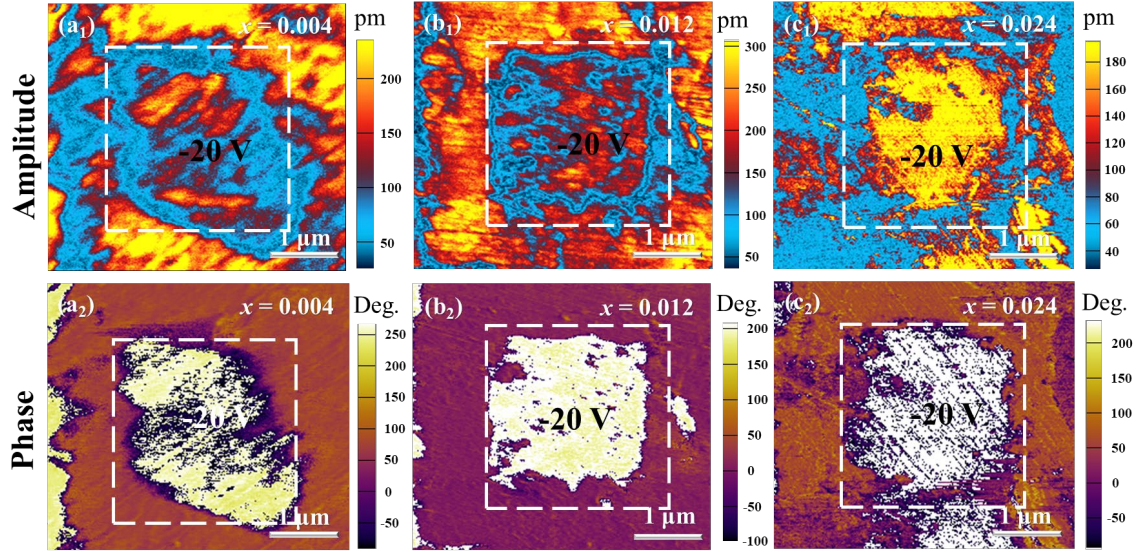


Fig. S8 Amplitude images of Litho mode at -20 V for (a₁) $x = 0.004$, (b₁) $x = 0.012$, and (c₁) $x = 0.024$; phase images of Litho mode at -20 V for (a₂) $x = 0.004$, (b₂) $x = 0.012$, and (c₂) $x = 0.024$.

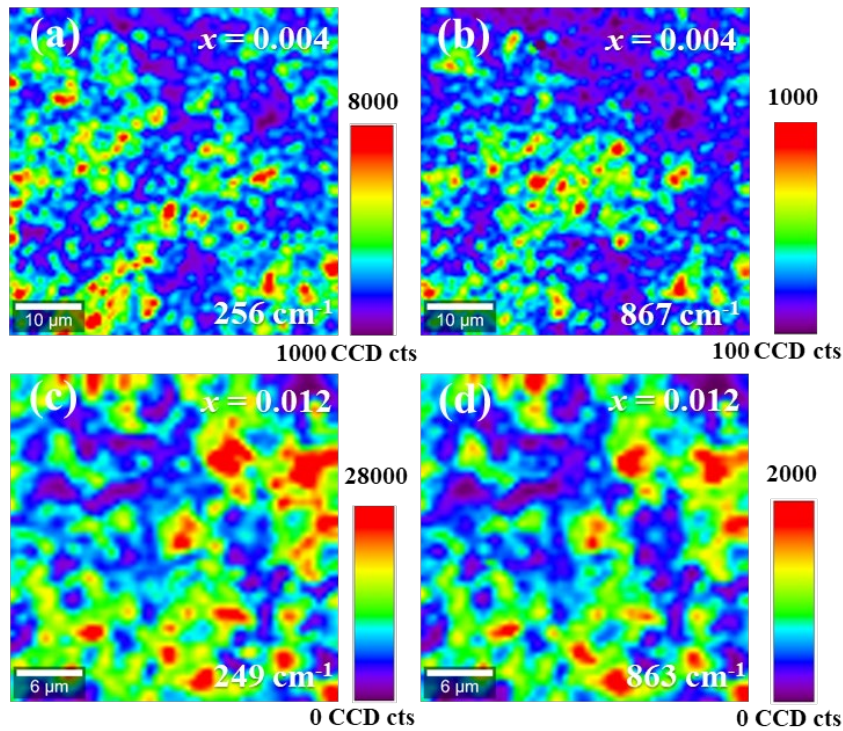


Fig. S9 The peak area of (a) the characteristic peak 256 cm^{-1} and (b) the characteristic peak 867 cm^{-1} of KNNT-BNZ-BFO/0.004 CSO ceramic is used as a parameter. The peak area of (c) the characteristic peak 249 cm^{-1} and (d) the characteristic peak 863 cm^{-1} of KNNT-BNZ-BFO/0.012 CSO ceramic is used as a parameter.

Fig. 5(d) presents the ϵ_r - T curve for ceramics in the temperature range of 30 to 500 °C. The ferroelectric to paraelectric phase-transition temperature (T_C) of ceramics

decreases with the increase of CSO doping content, which is attributed to the gradually destroyed LRFO and the promoted content of the local heterogeneity¹¹. Furthermore, the reduction of unit cell distortion can alleviate transformation stress during lattice deformation, resulting in a lower energy barrier for polarization variation between ferroelectric states. The temperature-dependent dielectric properties of the KNNT-BNZ-BFO/*x* CSO ceramics are analyzed using a modified Curie-Weiss law²¹⁻²³, as shown in Fig. S10(a-f). The diffuse-phase transition behavior of perovskite ferroelectrics can be expressed using this law, which relates the dielectric constant (ε) to temperature (T) and a constant (C). The modified Curie-Weiss law is shown in Equation 4.

$$\varepsilon = C / (T - T_0) \quad (4)$$

$$\Delta T_m = T_{cw} - T_m \quad (5)$$

$$\frac{1}{\varepsilon_r} - \frac{1}{\varepsilon_m} = \frac{(T - T_m)^\gamma}{C} \quad (6)$$

The change in diffuse phase transition behavior of the ceramics is evaluated using the values of ΔT_m and diffuseness index (γ)²⁴. ΔT_m is the difference between the transition temperature (T_m) and the Curie-Weiss temperature (T_{cw}), as shown in Equation 5. The γ is calculated using Equation 6, which relates the dielectric constants at the maximum (ε_m) and the transition (ε_r) temperatures to the temperature and the constant (C). Figure S10g shows the $\log(\frac{1}{\varepsilon_r} - \frac{1}{\varepsilon_m})$ as a function of $\log(T - T_m)$ curves, which can be used to evaluate the diffuseness of the ceramics. Generally, it is well known that the relaxor behavior in ferroelectrics is induced by PNRs, leading to a phase instability^{25, 26}. The diffuseness factor is used to describe the degree of relaxor: $\gamma = 1$ for normal ferroelectrics without PNRs existence, and $\gamma = 2$ for ideal relaxor ferroelectrics without long-range ferroelectric domains. From Fig. S10(g), the values of the diffuseness index (γ) gradually increase with an increasing x . This further illustrates the importance of Sb ions entering the lattice to replace Nb ions destroy the LRFO of the ceramics, thereby promoting the formation of high-density nanodomains along with PNRs, resulting in an increasement of relaxation behavior²⁷.

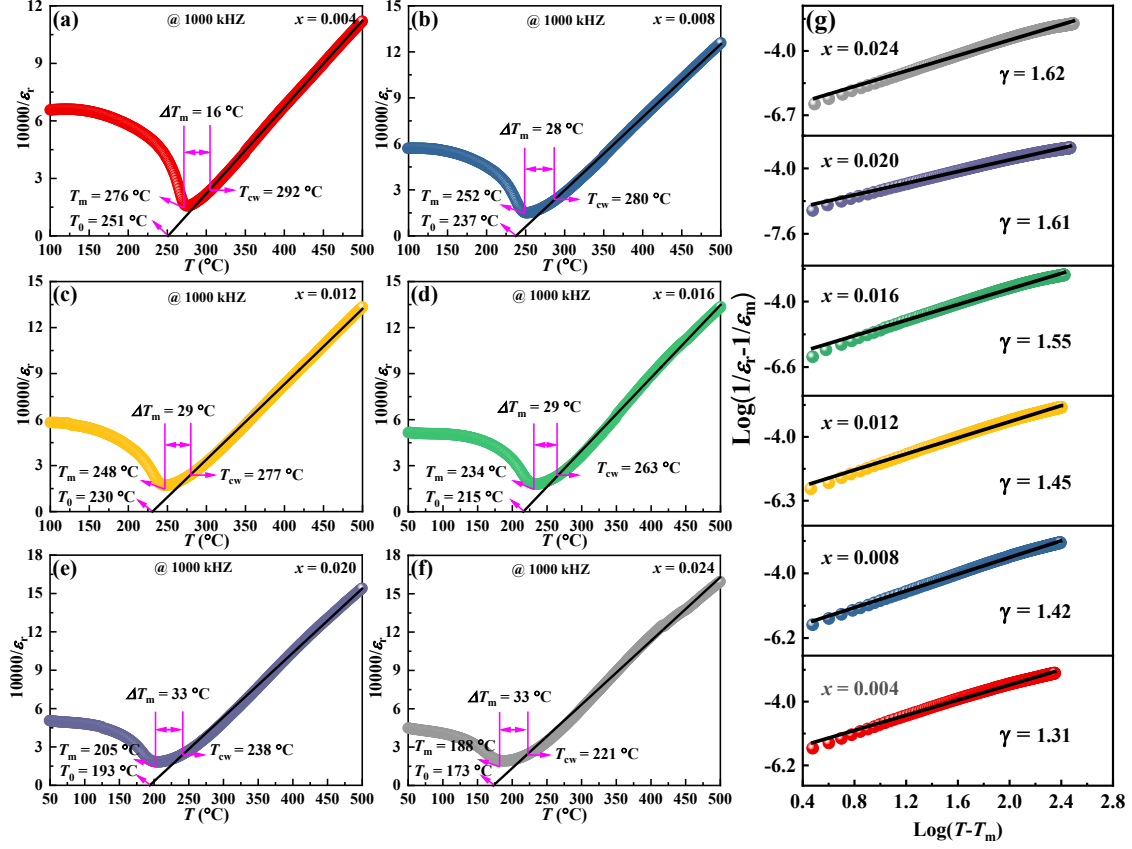


Fig. S10 (a-f) The relationship of the temperature and inverse dielectric permittivity of ceramics; (g) a plot of $\log(\frac{1}{\epsilon_r} - \frac{1}{\epsilon_m})$ as a function of $\log(T - T_m)$ for ceramics, and composition dependence of γ of the ceramics.

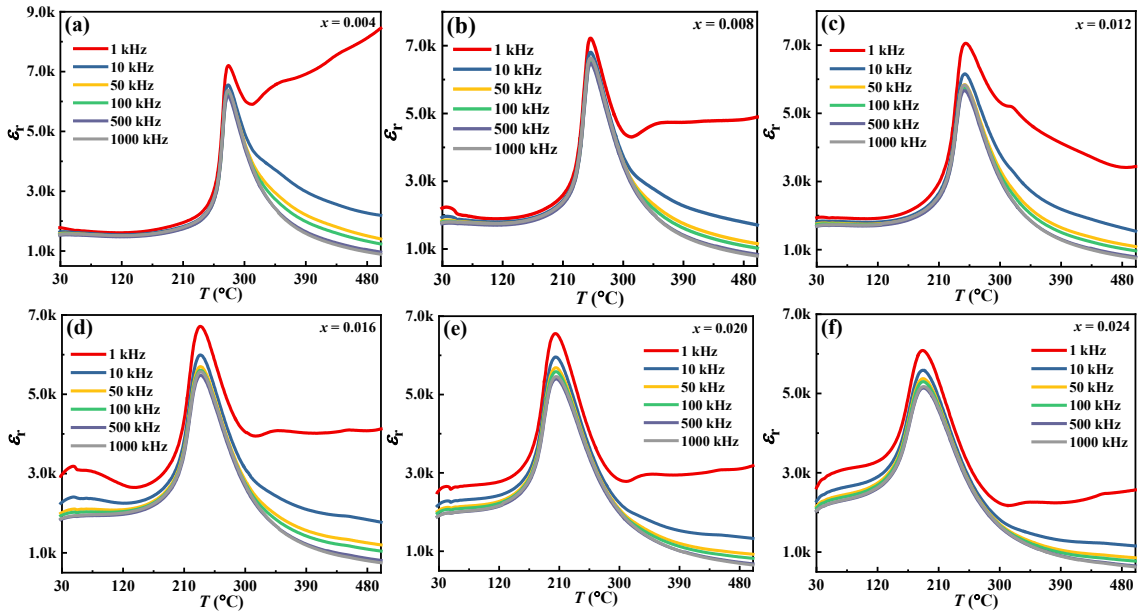


Fig. S11 ϵ_r - T curves for KNNT-BNZ-BFO/ x CSO composite ceramics in the temperature range from 30 to 500 °C.

The temperature-dependent electrical transport properties of the composites are shown in Fig. S12(d). The resistivity value decreases by orders of magnitude with an increase in temperature, confirming the negative temperature coefficient of the resistivity behavior similar to that of semiconductors²⁸. This is a process that is caused by a thermally activated charge carrier. The small-polaron hopping model is used for the investigation of the variation of the electrical resistivity²⁹⁻³¹. As can be seen in Fig. S12(e), the variation of the $\ln\rho$ of the composites with the inverse of temperature. The E_a and resistivity of KNNT-BNZ-BFO/0.004 CSO is smaller than that of KNNT-BNZ-BFO/0.012 CSO as can be seen from Fig. S12(d-e). This can be explained by the oxygen vacancies and grain size decrease, and the local stress field increase in the composites, resulting in an increase in E_a and resistivity. Fig. S12(f) illustrates the k_p of the composite ceramics decreases slightly at $x = 0.004-0.012$ and then considerably reduces with the addition of CSO. The $\tan\delta$ of the ceramic decreases with x increases, as shown in Fig. S12(f).

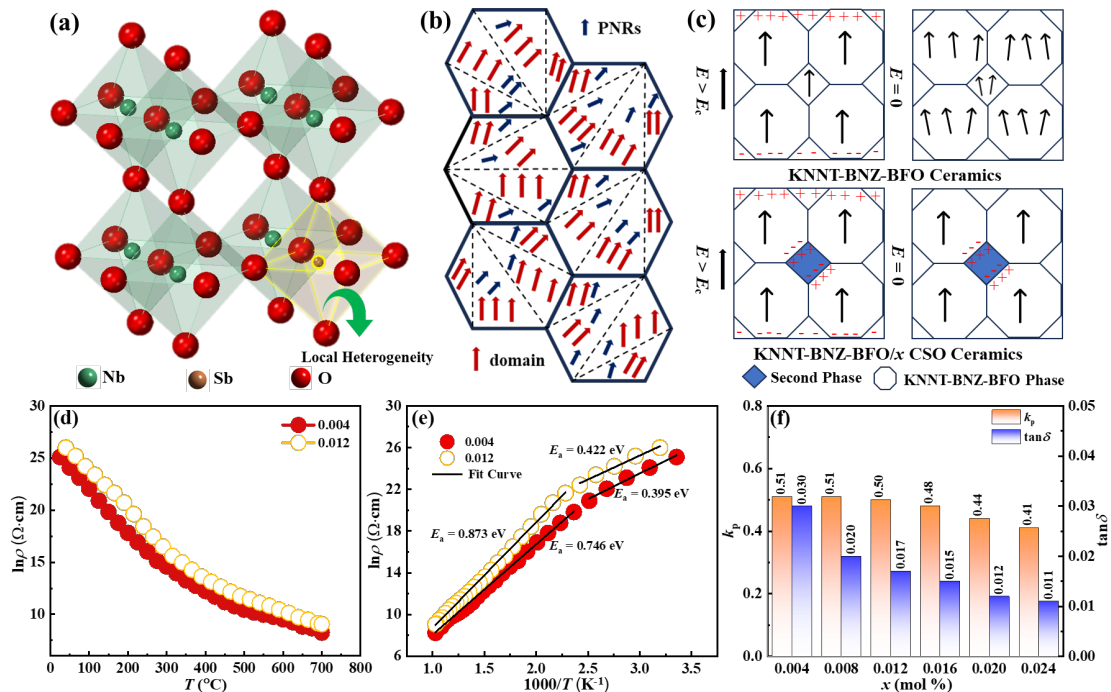


Fig. S12 (a) Schematic diagram of the lattice distortion induced by substituting Sb for Nb. (b) Domain evolution of composite ceramics. (c) The charge compensation model is seen in KNNT-BNZ-BFO/ x CSO composite ceramics. (d) Temperature dependence of the dc resistivity of KNNT-BNZ-BFO/ x CSO ($x = 0.004$ and 0.012) composite ceramics. (e) Resistance in the form of the natural logarithm vs. temperature. (f) k_p and $\tan\delta$ values as a function of CSO content.

Fig. S13(a) shows the switching of the current peaks becomes sharper and then flattens out in the electric field dependence of current (I - E) loops with the CSO content increases. This indicates that the addition of an appropriate amount of CSO can promote domain-switching behavior in the ceramics. The remanent polarization (P_r) value first increases and then decreases with increasing CSO content, as depicted in Figure S13b-c. Due to the higher covalency fraction of Sb-O bonds (61.69%) than that of Nb-O bonds (42.90%)¹⁴, the substitution of Sb^{5+} for Nb^{5+} promotes the hybridization of the B-site cation and O, the increase of covalency of Sb element can stiffen the B-O network and inhibit the ferroelectric distortion³². The long-range ferroelectric ordering in the KNNT-BNZ-BFO/ x CSO ceramics can be maintained at low Sb content, which is supported by their ϵ_r - T curves (Fig. S1(f)) and the high P_r values. In contrast, for the ceramics with a high Sb content, the further deteriorated LRFO and the promoted content of the local heterogeneity increase ϵ_r but sharply worsen P_r . An excess of the non-ferroelectric second phase leads to a decrease in the ferroelectricity of the ceramics, thus leading to decreased P_r values. Figure S13b-c shows the coercive field (E_c) value decreases gradually with the increasing x . The increase of the Sb ions entering the lattice to replace Nb ions content leads to the contraction of the BO_6 octahedra due to the difference in ionic radii between Sb^{5+} and Nb^{5+} , which results in the gradual disruption of the LRFO, the reduction of the unit cell distortion, and the enhancement of local structural heterogeneity^{11, 12}, as shown in Fig. S12(a-b). The reduction of the unit cell distortion indicates a decrease in crystalline anisotropy, which can result in a smaller free energy barrier among the ferroelectric/paraelectric phases³³. Decreased anisotropy of the free energy with polarization can be perceived when the energy barrier between various ferroelectric/paraelectric states decreases. A more ‘flattened’ energy profile can be established by reduced unit cell distortion³⁴. The induced ‘flattened’ energy profile contributes to the facilitation of the polarization variation. The hybridization between the B-site cation and O is critical to weaken the short-range repulsions and allow the ferroelectric transitions^{35, 36}. All of these factors contribute to structural flexibility,

which is characterized by a high dielectric constant (Fig. 5(d)) and low E_c ³³.

The strain properties of ferroelectrics are primarily determined by domain switching and domain wall motion, particularly in non-180° ferroelectric domains²⁴. The curves of the saturated butterfly-like strain (S - E) and the unipolar strain (S - E) are displayed in Figs. S13(d) and S13(e), respectively. The positive strain (S_{pos}) and unipolar strain (S_{uni}) have an initial increase followed by a decrease, and the reverse piezoelectric coefficients ($d_{33}^* = S_{\text{max}}/E_{\text{max}}$) initially increases from 383 pm/V to 390 pm/V and then decreases to 286 pm/V (Fig. S13(f)), while the negative strain (S_{neg}) gradually decreases with increasing CSO content. The reduction of unit cell distortion and the decreased energy barrier for polarization variation contribute to the increased strain properties^{21, 37}. However, the reduced S_{pos} , S_{uni} , and d_{33}^* values at CSO concentrations of 0.012-0.024 are mainly due to the strain incompatibility between the elastically-hard inclusions and the matrix, which can limit the strain response. This effect can be attributed to the strain incompatibility between the elastically hard inclusions and the matrix. The S_{neg} is attributed to the contribution of irreversible non-180° domain switching^{15, 38}. This is due to the destroyed ferroelectric domains, the pinning effects of the secondary phase, and the reduced grain size, which reduce the irreversible non-180° domain switching and the lattice distortion. The temperature-dependent P - E loops, I - E loops, saturated butterfly-like strain (S - E), and the unipolar strain (S - E) curves of KNNT-BNZ-BFO/0.012 CSO ceramic are measured within the temperature range of 30 to 130 °C are shown in Fig. S14. The local stress field inhibits the deformation of the crystal structure at high temperatures, thus exhibiting good temperature stability.

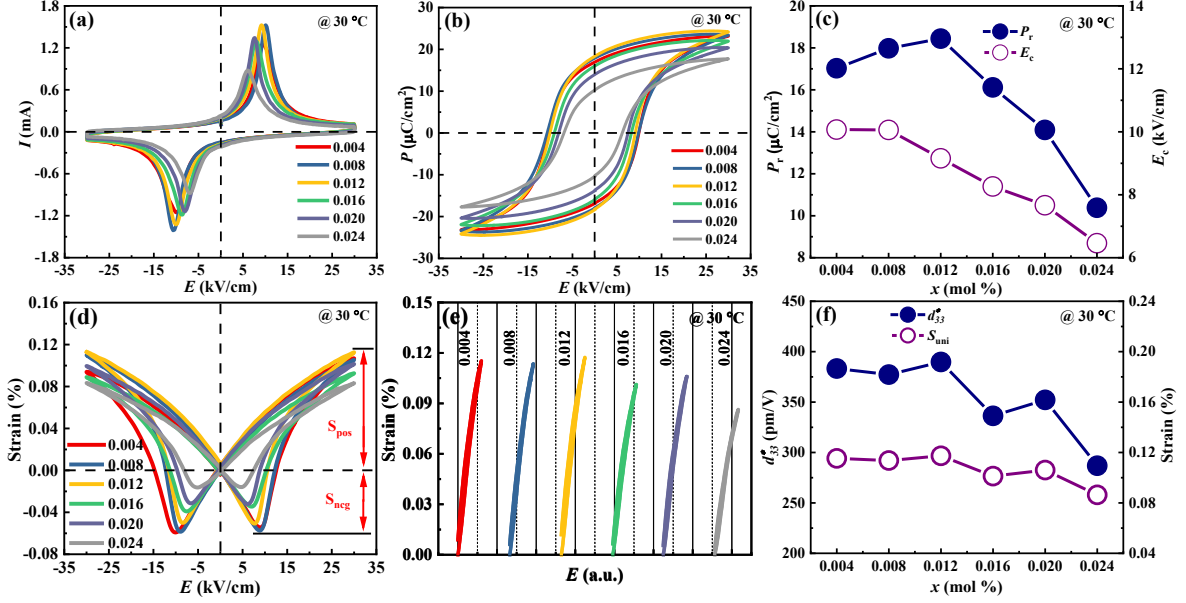


Fig. S13 (a) I - E curves; (b) P - E loops; (c) P_r and E_c values; (d) bipolar S - E curves; (e) unipolar S - E curves; (f) S_{uni} and d_{33}^* values as a function of CSO content.

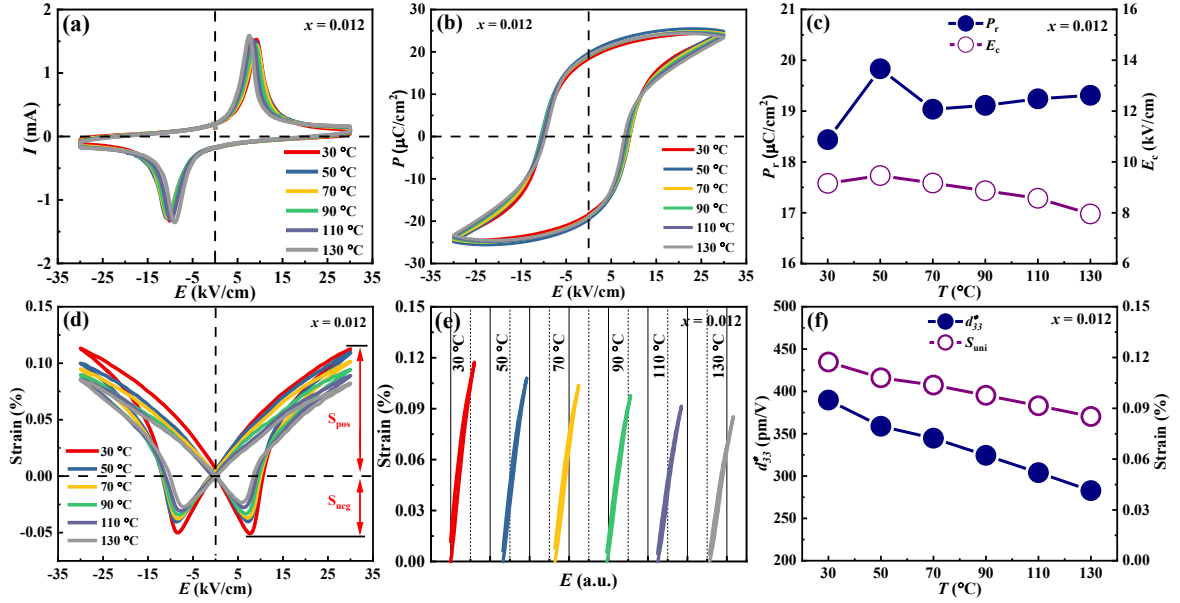


Fig. S14 (a) I - E curves; (b) P - E loops; (c) P_r and E_c values; (d) bipolar S - E curves; (e) unipolar S - E curves; (f) S_{uni} and d_{33}^* values of KNNT-BNZ-BFO/0.012 CSO sample as a function of temperature.

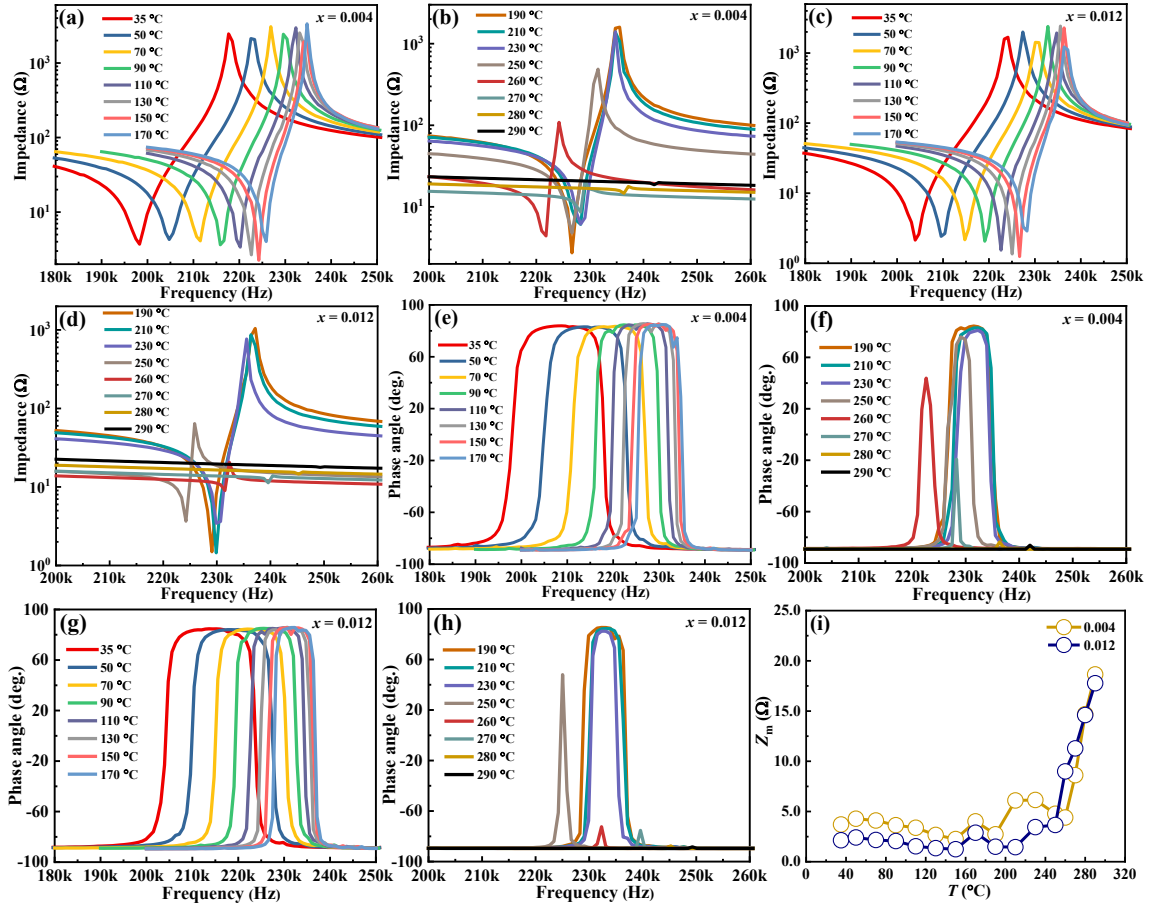


Fig. S15 *In-situ* temperature dependence of (a-d) the first radial mode frequency shift, (e-h) phase angle, and (i) Z_m of the KNNT-BNZ-BFO/ x CSO ($x = 0.004$ and 0.012) composite ceramics measured from 35 to 290 °C.

In the thermodynamic theory of ferroelectrics, the piezoelectric properties are closely related to the ferroelectric, dielectric, and electrostrictive properties^{39, 40}. Generally, the relationship among d_{33} , ϵ_r , and P_r for piezoelectric ceramics (where $\epsilon_r = \epsilon_{33}$, $P_r = P_3$) according to the formula $d_{33} = 2Q_{33} \cdot \epsilon_0 \cdot \epsilon_r \cdot P_r$ ⁴¹ (Fig. S16). Therefore, high d_{33} and k_p values are maintained for the ceramics with $x = 0.004$ - 0.012 , which are based on the well-maintained LRFO as well as could be further enhanced by the R-T multiphase coexistence, space charges hinder domains back-switching, and moderate PNRs contribute to the increased ϵ_r and the P_r . In contrast, for the ceramics with a high Sb content, the further deteriorated LRFO and the promoted content of the local heterogeneity increase ϵ_r but sharply worsen P_r . An excess of the non-ferroelectric second phase leads to a decrease in the ferroelectricity of the ceramics, thus leading to the decreased d_{33} and $\epsilon_r P_r$ values.

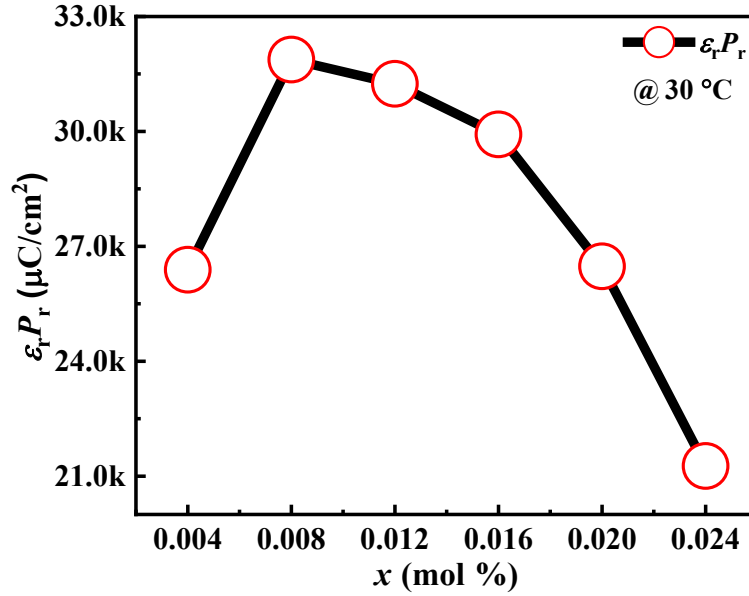


Fig. S16 Composition dependency of $\epsilon_r P_r$.

Figs. S17(a) and S17(b) show the load-depth curves for the KNNT-BNZ-BFO/ x CSO ($x = 0.004$, and 0.012) ceramics. The maximum depth (h_m) value at each peak load of KNNT-BNZ-BFO/ 0.012 CSO is smaller than that of KNNT-BNZ-BFO/ 0.004 CSO. An anomaly characterized by a sudden softening and minimization of the energy storage modulus (E') at the ferroelectric to paraelectric phase-transition temperature (T_c) is observed during the heating process. This anomaly commences at approximately 260 °C and approximately 230 °C for the ceramics with $x = 0.004$ and $x = 0.012$, respectively. The onset temperature of the elastic anomaly (mechanical softening) is lower than the temperature corresponding to the dielectric peak, which possibly originates from an intrinsic phase transition mechanism⁴². The elastic modulus is always the lowest for a given ferroelectric phase before the phase transition when the potential energy surface is at its lowest and flattest. The elastic modulus is at its lowest when the phase transition is about to take place. However, once the phase transition occurs, the cubic (C) phase loses its ferroelectric polarization and corresponding strain, and then the elastic modulus rises rapidly. The reason why the elastic anomaly signals the onset of the ferroelectric to C phase transition instead of the average transition must be the sensitivity of E' to the

ferroelectric/ferroelastic activity. Whereas the permittivity of perovskite systems is associated with the ordered-disordered phase transition mechanism. The phase transition from low to high temperatures always leads to an increase in the permittivity, and it is only after the phase transition occurs that the permittivity becomes higher. This phenomenon can be understood by the eight-site model, the B-site atom at a high-temperature phase can occupy more sites, and thus it is easier to induce electric polarization under an external electric field. The elastic anomalies signal the onset of the ferroelectric to C phase transition on heating, while the dielectric anomalies take place at the average temperature⁴².

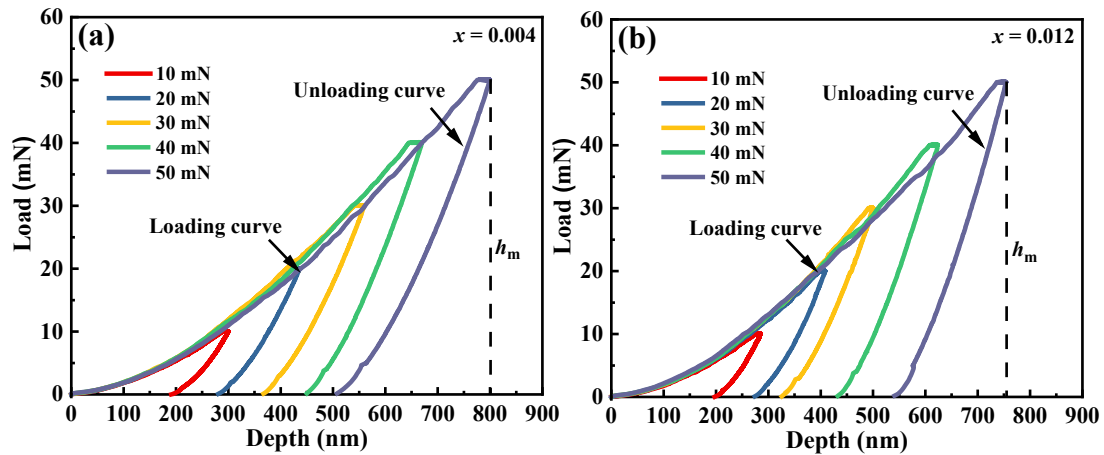


Fig. S17 Load-depth curves for (a) $x = 0.004$ and (b) $x = 0.012$.

For device applications, the temperature stability of piezoelectric properties is an important factor to consider. In this study, the *in-situ* temperature-dependent k_p and Q_m of the KNNT-BNZ-BFO/ x CSO ($x = 0.004$ and 0.012) composite ceramics are measured, and the results are presented in Fig. S18(a-b). We further compared the *in-situ* temperature-dependent d_{33} of the KNNT-BNZ-BFO/0.012 CSO composite ceramic with that of the KNNT-BNZ-BFO ceramic¹, as illustrated in Fig. S18(c). Interestingly, the KNNT-BNZ-BFO/0.012 CSO sample not only exhibits superior electromechanical compatibility compared to the KNNT-BNZ-BFO sample but also demonstrates more excellent temperature stability. This highlights the promising potential of the KNNT-BNZ-BFO/0.012 CSO composite ceramic for practical

applications. In poled KNN-based piezoelectric materials, the high temperature will favor the motion of the dipole and atoms, and the strong thermal fluctuation can break the ferroelectric order and motivate the migration of the domain wall. Some poled domains with metastability will therefore return to the initial state, leading to depolarization and a lower d_{33} value. To study the effect of phase transition on temperature stability, *in-situ* variable temperature XRD tests are conducted, as shown in Fig. S18(d-i). During heating, phase evolution occurs, leading to lattice deformation that can affect piezoelectric performance. From Figs. S18(f) and S18(i), it can be observed that the $x = 0.012$ sample experiences less lattice distortion with increasing temperature compared to the $x = 0.004$ sample. In this work, the presence of remnant stress fields at KNNT-BNZ-BFO/secondary phase interfaces mitigates the distortion of the lattice and the domain reorientation during the heating process^{20, 43, 44}. Therefore, the KNNT-BNZ-BFO/0.012 CSO ceramic as a whole demonstrates better temperature stability of d_{33} at the macroscopic level.

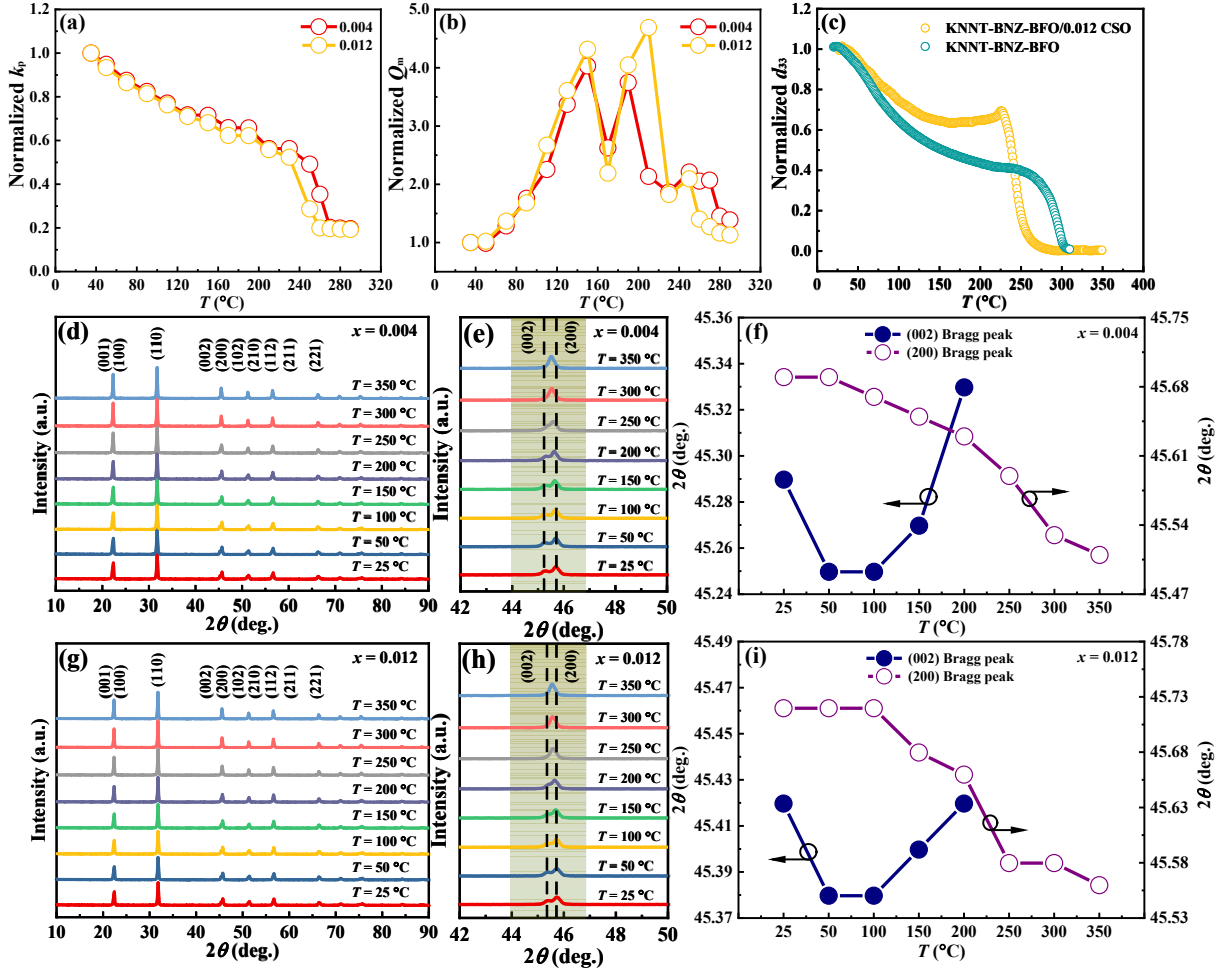


Fig. S18 *In-situ* temperature stability of (a) k_p , and (b) Q_m for KNNT-BNZ-BFO/ x CSO ($x = 0.004$ and 0.012) composite ceramics. (c) *In-situ* temperature stability of d_{33} for KNNT-BNZ-BFO/ 0.012 CSO composite ceramic and KNNT-BNZ-BFO ceramic¹. *In-situ* XRD patterns of ceramics measured at different temperatures at (d) $2\theta = 10-90^\circ$, (e) $2\theta = 42-50^\circ$, (f) shift of (002) and (200) Bragg peaks as a function of temperature for $x = 0.004$; (g) $2\theta = 10-90^\circ$, (h) $2\theta = 42-50^\circ$, (i) shift of (002) and (200) Bragg peaks as a function of temperature for $x = 0.012$.

References

1. H. Li, L. Xie, Z. Tan, J. Xing, X. Li, H. Chen, F. Wang, Y. Cheng, M. Tang and J. Zhu, *Inorganic Chemistry*, 2022, 61, 18660-18669.
2. H. Li, H. Chen, X. Li, J. Xing, W. Liu, Zhi Tan, M. Mo, N. Chen, M. Tang and J. Zhu, *ACS Applied Materials & Interfaces*, 2023, 15, 36576-36586.
3. H. Li, N. Chen, J. Xing, H. Chen, Z. Tan, M. Mo, Q. Chen, J. Zhu, F. Li, Z. Liu, W. Ouyang and H. Zhu, *Journal of Materials Chemistry C*, 2024, 12, 1809-1819.
4. S. Zhang, E. F. Alberta, R. E. Eitel, C. A. Randall and T. R. Shrout, *Ieee Transactions on Ultrasonics Ferroelectrics and Frequency Control*, 2005, 52, 2131-2139.
5. L. M. Riemer, K. V. Lalitha, X. J. Jiang, N. Liu, C. Dietz, R. W. Stark, P. B. Groszewicz, G. Buntkowsky, J. Chen, S. T. Zhang, J. Rodel and J. Koruza, *Acta Mater.*, 2017, 136, 271-280.
6. R. W. Davidge and T. J. Green, *J. Mater. Sci.*, 1968, 3, 629-634.

7. J. Xing, M. Mo, Y. Cheng, Z. Tan and J. Zhu, *The Journal of Physical Chemistry C*, 2024, 128, 658-666.
8. M. Fukuda, I. Yamada, H. Murata, H. Hojo, O. J. Hernandez, C. Ritter, K. Tanaka and K. Fujita, *Chemistry of Materials*, 2020, 32, 5016-5027.
9. L. Qiao, G. Li, H. Tao, J. Wu, Z. Xu and F. Li, *Ceramics International*, 2020, 46, 5641-5644.
10. Z.-D. He, W.-C. Li, J.-L. Yang, H.-K. Xu, X.-F. Xu, G.-X. Lai, Y.-D. Che, W.-L. Zhu, X.-D. Yang and X.-Y. Chen, *RSC Advances*, 2023, 13, 34475-34481.
11. N. Zhang, X. Lv, X.-x. Zhang, A. Cui, Z. Hu and J. Wu, *ACS Applied Materials & Interfaces*, 2021, 13, 60227-60240.
12. Y. Li, A. Cui, K. Dai, Y. Yan, K. Jiang, L. Shang, L. Zhu, Y. Li, J. Zhang, X. Lv, J. Wu and Z. Hu, *Acta Materialia*, 2024, 265, 119612.
13. A. P. Espinosa, L. Ramajo, F. Rubio-Marcos, C. Macchi, A. Somoza and M. Castro, *Journal of the European Ceramic Society*, 2021, 41, 1288-1298.
14. Y. Zhang and J.-F. Li, *Journal of Materials Chemistry C*, 2019, 7, 4284-4303.
15. A. Song, Y. Liu, T. Feng, H. Li, Y. Zhang, X. Wang, L. Liu, B. P. Zhang and J. F. Li, *Advanced Functional Materials*, 2022, 32, 2204385.
16. T. Wang, C. Wu, J. Xing, J. Wu, B. Li-Chen, X. Xu, K. Wang and J. Zhu, *Journal of the American Ceramic Society*, 2019, 102, 6126-6136.
17. L. Wu, T. Zheng and J. Wu, *Journal of the European Ceramic Society*, 2022, 42, 4888-4897.
18. C. Chen, L. Yang, X. Jiang, X. Huang, X. Gao, N. Tu, K. Shu, X. Jiang, S. Zhang and H. Luo, *Crystals*, 2020, 10, 435.
19. B. Wu, J. Ma, W. Wu and M. Chen, *Journal of Materials Chemistry C*, 2020, 8, 2838-2846.
20. K. Xi, Y. Hou, X. Yu, M. Zheng and M. Zhu, *Journal of Materials Chemistry A*, 2023, 11, 3556-3564.
21. J. Xing, S. Xie, B. Wu, Z. Tan, L. Jiang, L. Xie, Y. Cheng, J. Wu, D. Xiao and J. Zhu, *Scripta Materialia*, 2020, 177, 186-191.
22. J. Xing, Z. Tan, L. Xie, L. Jiang, J. Yuan, Q. Chen, J. Wu, W. Zhang, D. Xiao and J. Zhu, *Journal of the American Ceramic Society*, 2018, 101, 1632-1645.
23. M.-H. Zhang, Q. Zhang, T.-T. Yu, G. Li, H.-C. Thong, L.-Y. Peng, L. Liu, J. Ma, Y. Shen, Z. Shen, J. Daniels, L. Gu, B. Han, L.-Q. Chen, J.-F. Li, F. Li and K. Wang, *Materials Today*, 2021, 46, 44-53.
24. X. Ren, Z. Peng, B. Chen, Q. Shi, X. Qiao, D. Wu, G. Li, L. Jin, Z. Yang and X. Chao, *Journal of the European Ceramic Society*, 2020, 40, 2331-2337.
25. F. Li, S. Zhang, D. Damjanovic, L.-Q. Chen and T. R. ShROUT, *Advanced Functional Materials*, 2018, 28, 1801540.
26. G. Xu, J. Wen, C. Stock and P. M. Gehring, *Nature Materials*, 2008, 7, 562-566.
27. N. Zhang, T. Zheng, N. Li, C. Zhao, J. Yin, Y. Zhang, H. Wu, S. J. Pennycook and J. Wu, *ACS Applied Materials & Interfaces*, 2021, 13, 7461-7469.
28. Q. Xu, M. T. Lanagan, W. Luo, L. Zhang, J. Xie, H. Hao, M. Cao, Z. Yao and H. Liu, *Journal of the European Ceramic Society*, 2016, 36, 2469-2477.
29. T. A. Abtew, M. Zhang and D. A. Drabold, *Physical Review B*, 2007, 76, 045212.

30. G. Liu, S. Ren, C. Wu, D. Wang, F. Li, J. Wu and Q. Chen, *Journal of the American Ceramic Society*, 2018, 101, 4615-4626.
31. H. Li, G. Dong, K. Chu, X. Pu, Z. Li, H. Zhang, Q. Chen and X. Liu, *Journal of Materials Chemistry C*, 2020, 8, 17054-17064.
32. A. Villesuzanne, C. Elissalde, M. Pouchard and J. Ravez, *THE EUROPEAN PHYSICAL JOURNAL B*, 1998, 6, 307-312.
33. Q. Liu, Y. Zhang, J. Gao, Z. Zhou, D. Yang, K.-Y. Lee, A. Studer, M. Hinterstein, K. Wang, X. Zhang, L. Li and J.-F. Li, *National Science Review*, 2020, 7, 355-365.
34. W. Liu and X. Ren, *Physical Review Letters*, 2009, 103, 257602.
35. R. E. Cohen, *Nature*, 1992, 358, 136-138.
36. K. Miura, M. Azuma and H. Funakubo, *Materials*, 2011, 4, 260-273.
37. X. Lv, N. Zhang, Y. Ma, X.-x. Zhang and J. Wu, *Journal of Materials Science & Technology*, 2022, 130, 198-207.
38. Z. Cen, Y. Yu, P. Zhao, L. Chen, C. Zhu, L. Li and X. Wang, *Journal of Materials Chemistry C*, 2019, 7, 1379-1387.
39. I. Fujii, S. Ueno and S. Wada, *Journal of the European Ceramic Society*, 2020, 40, 2970-2976.
40. P. Li, Z. Fu, F. Wang, Y. Huan, Z. Zhou, J. Zhai, B. Shen and S. Zhang, *Acta Materialia*, 2020, 199, 542-550.
41. F. Li, D. Lin, Z. Chen, Z. Cheng, J. Wang, C. Li, Z. Xu, Q. Huang, X. Liao, L.-Q. Chen, T. R. Shroud and S. Zhang, *Nature Materials*, 2018, 17, 349-354.
42. A. M. Mazuera, P. S. Silva, A. D. Rodrigues, P. S. Pizani, Y. Romaguera-Barcelay, M. Venet and M. Algueró, *Physical Review B*, 2016, 94, 184101.
43. H. Zhao, Y. Hou, X. Yu, M. Zheng and M. Zhu, *Acta Materialia*, 2019, 181, 238-248.
44. X. Yu, Y. Hou, M. Zheng and M. Zhu, *Journal of Materials Chemistry A*, 2021, 9, 26741-26749.